Reaction Mechanism of Hydrogen Generation and Nitrogen Fixation at Carbon Nitride/Double Perovskite Heterojunctions

Costanza Tedesco,[a] Luca Gregori,[b] Angelica Simbula,[c] Federico Pitzalis,[c] Andrea Speltini,[a] Francesca Merlo,[a] Silvia Colella,[d] Andrea Listorti,[e] Edoardo Mosconi,[f,g] Asma A. Alothman,[g] Waldemar Kaiser,[f] Michele Saba,[b] Antonella Profumo,[a] Filippo De Angelis,[b,f,g,h] Lorenzo Malavasi[a,*]*

[a]Department of Chemistry and INSTM, University of Pavia,Via Taramelli 16, Pavia, 27100, Italy
[b]Department of Chemistry, Biology and Biotechnology, University of Perugia and INSTM, Via Elce di Sotto 8, 06123 Perugia, Italy
[c]Dipartimento di Fisica, Università di Cagliari, 09042 Monserrato, Italy
[d]CNR NANOTEC - c/o Dipartimento di Chimica, Università di Bari, Via Orabona 4, 70126 Bari, Italy
[e]Department of Chemistry, University of Bari "Aldo Moro", via Orabona 4, 70126, Bari, Italy
[f]Computational Laboratory for Hybrid/Organic Photovoltaics (CLHYO), Istituto CNR di Scienze e Tecnologie Chimiche "Giulio Natta" (CNR-SCITEC), Via Elce di Sotto 8, 06123 Perugia, Italy
[g]Chemistry Department, College of Science, King Saud University, Riyadh 11451, Kingdom of Saudi Arabia
[h]SKKU Institute of Energy Science and Technology (SIEST) Sungkyunkwan University, Suwon, Korea 440-746

Corresponding Authors

Edoardo Mosconi, email: edoblasco@gmail.com

Lorenzo Malavasi, email: lorenzo.malavasi@unipv.it

ABSTRACT

Photocatalytically active heterojunctions based on metal halide perovskites (MHPs) are drawing significant interest for their chameleon ability to foster several redox reactions. The lack of mechanistic insights into their performance, however, limits the ability of engineering novel and optimized materials. Herein, we report on a composite system including a double perovskite, $Cs_2AgBiCl_6$/g-C_3N_4, used in parallel for solar-driven hydrogen generation and nitrogen reduction. The composite efficiently promotes the two reactions, but its activity strongly depends on the perovskite/carbon nitride relative amounts. Through advanced spectroscopic investigation and density function theory modelling we studied the H_2 and NH_3 production reaction mechanisms, finding perovskite halide vacancies as the primary reactive sites for hydrogen generation, withstanding a positive contribution of low loaded g-C_3N_4, in reducing carrier recombination. For nitrogen reduction, instead, the active sites are g-C_3N_4 nitrogen vacancies, and the heterojunction best performs at low perovskites loadings, as the composites maximizes light absorption and reduced carrier losses. We believe these insights are important add-ons towards universal exploitation of MHPs in contemporary photocatalysis.

Photocatalytic reactions mediated by metal halide perovskites (MHPs) have become a topic of current interest because of the promise of improved low-cost devices for solar fuel production.[1–8] Thanks to their excellent optoelectronic properties, namely tunable band gap, high absorption coefficient, low exciton binding energy, and high carrier mobility, MHPs were successfully applied to a wide range of photocatalytic reactions. Furthermore, a suitable band alignment of MHPs with the most common redox half-reactions allows to run both reduction and oxidation reactions,[1] as confirmed by the recent experimental demonstrations of the two most representative examples, namely hydrogen photogeneration and CO_2 reduction.[1–3,9–15]

With respect to traditional metal oxides photocatalysts, MHPs present a large chemical and structural variety, which allows the design and tailoring the material composition for the envisaged solar-drive reaction. In this respect, both lead-based and lead-free systems have been explored, ranging from 3D to 2D perovskites, perovskite derivatives of general formula $A_3B_2X_9$, and $A_2(BB')X_6$ double perovskites.[16–25]

The general strategy to realize a spatial separation of photo-excited electron-hole pairs in MHPs-based photocatalysts is to design suitable heterojunctions by coupling two semiconductors.[26,27] In addition, the second semiconductor can also act as co-catalyst to improve surface reaction.[28] Again, the high tunability of MHPs allows the design of materials with suitable conduction band (CB) and valence band (VB) offsets to achieve the heterojunction and to provide enough overpotential to drive the target photoreaction.

In recent years, several type II and Z-scheme heterojunction including MHPs have been reported for a range of photocatalytic reactions. The partner semiconductor of choice, in most cases, has been graphitic carbon nitride (g-C_3N_4).[16–18,29–35] g-C_3N_4 is one of the most appealing and performing metal-free photocatalysts having a good absorption in the visible spectrum (band gap of about 2.7 eV), ease of preparation from cheap precursors, it is atoxic, and is stable in both acidic and basic media.[36] In MHPs/g-C_3N_4 heterojunctions, photogenerated electrons tend to migrate and accumulate in g-C_3N_4, where active sites for the photocatalytic reaction are

present, while holes from graphitic carbon nitride migrate to the MHP. On the other hand, the perovskite itself can efficiently photogenerate hydrogen by hydrohalic acid splitting, as demonstrated in $MAPbI_3$ (MA=methylammonium) and then in other systems such as $CsPbBr_3$.[20,37] Moving away from toxic lead, Bi-based perovskite derivatives were also successfully employed in heterojunctions for hydrogen photogeneration.[18,31,35] More recently, significant interest has been triggered by Bi-based double perovskites for their potential use in different photocatalytic reactions, thanks to their superior stability, wide compositional tunability, and good optical properties. $Cs_2AgBiBr_6$ has been investigated for photocatalytic CO_2 reduction, where it has been found that the surface of the perovskites acts as reaction site in the reduction process.[23,33] Fewer reports refer to the hydrogen generation mediated by this double perovskites, with the $NiCoP/Cs_2AgBiBr_6$ heterojunction representing the best report to date with about 400 μmol g^{-1} h^{-1} of evolved hydrogen under 300 W illumination at $\lambda \geq 420$ nm.[38] The proposed mechanism in this system considers an effective transfer of electrons from $Cs_2AgBiBr_6$ to the CB of NiCoP on which the H_2 generation reaction occurs.[38]

While there is an increasing amount of evidence about the effective role of MHPs and MHP-based heterojunctions in running various photocatalytic processes, a detailed description of the reaction mechanism(s) is still lacking. For this reason, herein, we report a combined experimental and computational study on $Cs_2AgBiCl_6/g\text{-}C_3N_4$ heterojunctions which has been applied to run two different photocatalytic reactions: hydrogen generation and nitrogen reduction to ammonia, to the best of our knowledge. This last reaction has never been explored before in any MHP-based system. $Cs_2AgBiCl_6$ has been selected based on its optimal moisture stability, suitable band alignment and because it is a lead-free compound. The $Cs_2AgBiCl_6/g\text{-}C_3N_4$ composite system has been investigated in the whole weight ratio between perovskite and $g\text{-}C_3N_4$. We found that MHP-rich compositions perform better in the H_2 photogeneration, while $g\text{-}C_3N_4$-rich systems are more effective in the nitrogen photofixation reaction. As reported above, due to the limited microscopic details about the photocatalytic activity of MHP-based

heterojunctions, key aim of this work is to provide a comprehensive description of the mechanism underpinning the solar-light mediated reactions in terms of charge carrier dynamics and reaction active sites. This has been achieved through a detailed photophysical and computational modelling study on the prepared systems and for the two photocatalytic reactions investigated providing solid clues about reaction mechanisms. While the application of MHPs-based heterojunction for hydrogen photogeneration is now quite well established, the present work clarifies the suitability of such composite systems to run nitrogen reduction reaction, exploring a new avenue in the photocatalytic application of MHPs.

Results and Discussion

The $Cs_2AgBiCl_6$/g-C_3N_4 systems have been synthesized according to the experimental procedure reported in the Supplementary Information (SI). Weight ratios investigated between $Cs_2AgBiCl_6$ and g-C_3N_4 nanosheets are (wt% of perovskite) 100, 99, 97.5, 95, 90, 85, 82.5, 80, 70, 50, 25, 10, 2.5, and 0. Figure 1a reports the room temperature X-ray diffraction patterns of some selected compositions investigated (corresponding to the best performances, see later in the text).

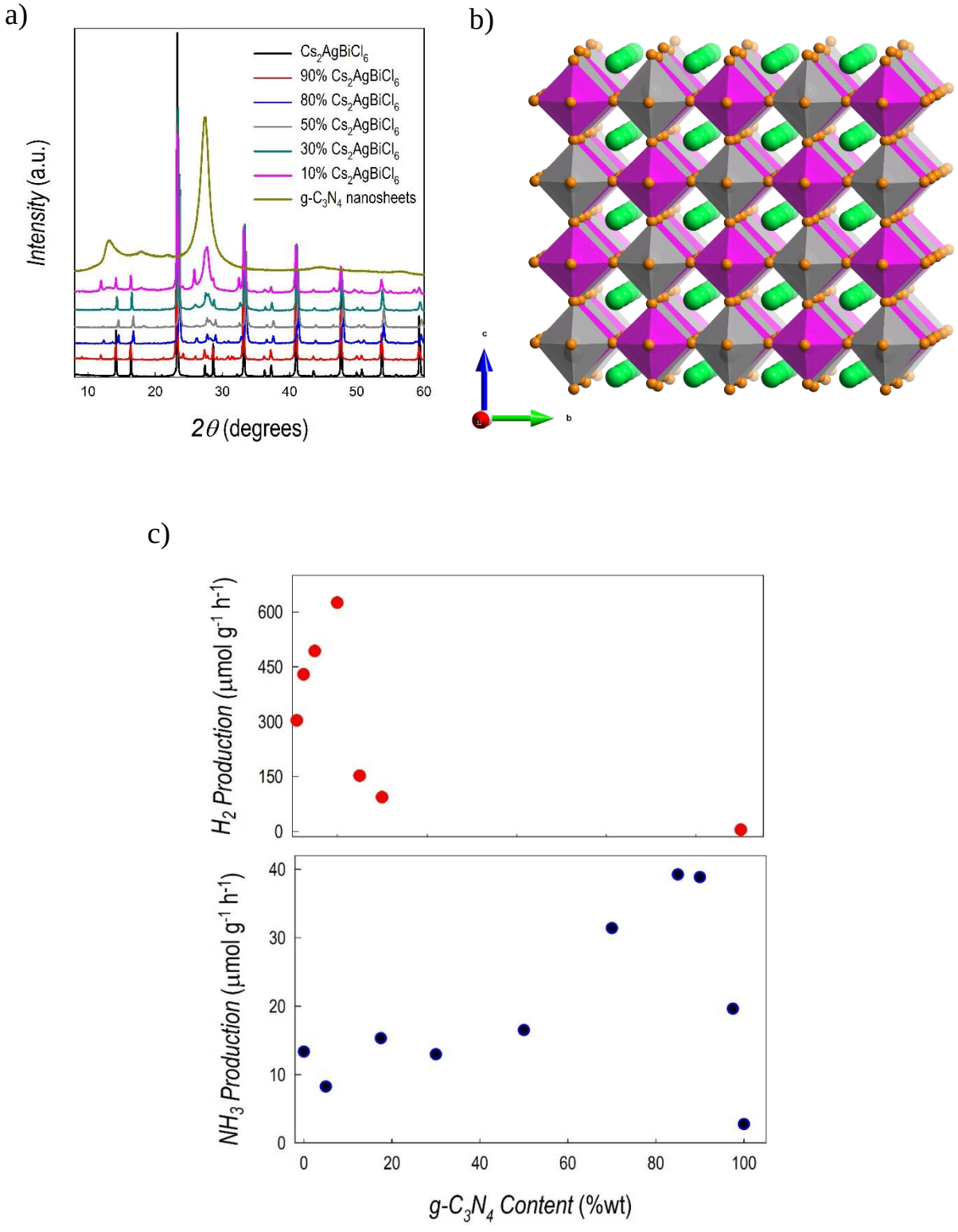

Figure 1. **Structural properties and photocatalytic performance of $Cs_2AgBiCl_6$/g-C_3N_4 composites** **a** XRD pattern of selected $Cs_2AgBiCl_6$/g-C_3N_4 composites; **b** sketch of $Cs_2AgBiCl_6$ crystal structure where Cs^+ ions are shown as green spheres, the chloride ions as orange spheres, while the Ag and Bi octahedra are shown as silver and purple polyhedra, respectively; **c** hydrogen and ammonia productions as a function of g-C_3N_4 wt% in the composites. (*n=3*, simulated solar light, 500 W m^{-2}).

In the bottom part of Figure 1a, the pattern of $Cs_2AgBiCl_6$ double perovskite is reported (with a sketch of its crystal structure in Figure 1b), displaying a cubic symmetry with *Fm3̄m* space group (#225) and a lattice parameter of 10.7761(2) Å, in agreement with previous results.[39] Figure S1 shows a comparison between experimental and calculated pattern for $Cs_2AgBiCl_6$. At the top of Figure 1a, the X-ray pattern of pure g-C_3N_4 nanosheets is reported showing the typical broad peaks around 13° and 28° corresponding to the (100) and (002) reflections.[40] The patterns of the composites (cfr. Figure 1b) are dominated by perovskite reflections at high wt% of $Cs_2AgBiCl_6$ and the reflections of g-C_3N_4 start to be evident around 50 wt%. Also, at 10 wt% of perovskite its pattern is still clearly detectable, due to its high scattering power with respect to g-C_3N_4. Morphological inspection of $Cs_2AgBiCl_6$, g-C_3N_4, and selected composites has been carried out by Scanning Electron Microscopy (SEM) and the results are reported in Figure S2. g-C_3N_4 nanosheets have been also characterized by Transmission Electron Microscopy (TEM) and representative images showing their nanostructure are shown in Figure S3.

Figure 1c reports the results in terms of hydrogen and ammonia evolution rates (top and bottom graphs, respectively), expressed as μmol g^{-1} h^{-1}, obtained by photocatalytic experiments under simulated solar light (for details see Methods section). The two production rates follow opposite trends as a function of composition, with perovskite-rich samples performing better for the hydrogen generation and perovskite-poor ones running the nitrogen reduction more efficiently. The trend of hydrogen evolution rate (HER), deriving from HCl splitting, steeply increases from pure $Cs_2AgBiCl_6$ to the composite including 10wt% of g-C_3N_4, reaching a value of 625 μmol g^{-1} h^{-1} which is more than double with respect to pure perovskite. Note that pure g-C_3N_4, under these reaction conditions, provide an HER of 4 μmol g^{-1} h^{-1}. The reported data confirm a synergistic effect of the composite in enhancing the photocatalytic HCl splitting ability of $Cs_2AgBiCl_6$, thanks to the formation of an effective heterojunction (see later in the text). The present results, while being the first related to the hydrogen generation by

$Cs_2AgBiCl_6$, can be compared to analogous sytems involving double perovskites. To date, only the HBr splitting by $Cs_2AgBiBr_6$ has been explored in heterojunctions with reduced graphene oxide, NiCoP or nitrogen-doped carbon.[38,41,42] The best HER has been reported for the $Cs_2AgBiBr_6$/2.5%RGO system providing around 490 μmol g^{-1} h^{-1} of hydrogen under solar illumination in HBr.[41] With the present $Cs_2AgBiCl_6$/10% g-C_3N_4 composite we are reporting the highest hydrogen photogeneration, around 625 μmol g^{-1} h^{-1} for a system including a lead free double perovskite through the efficient HCl splitting which could be of more applicative potential with respect to the splitting of HBr or HI reported so far.[9]

The reduction of nitrogen to ammonia, as mentioned, follows a different trend with respect to the composition (Figure 1c), with a gradual increase of the NH_3 generation rate starting from pure $Cs_2AgBiCl_6$ up to the $Cs_2AgBiCl_6$/90% g-C_3N_4 composite, reaching a maximum value of about 40 μmol g^{-1} h^{-1}. Pure g-C_3N_4 nanosheets or lower amounts of perovskite in the composite (see the point at 5wt%) perform significantly less effectively. Also in this case, by looking at the nitrogen fixation results of the pure compounds, it is possible to unveil an effective synergy between the two semiconductors. As mentioned, there are no previous reports about nitrogen reduction by an MHP-based heterojunction. However, g-C_3N_4 has been reported as a suitable material for this reaction, in particular thanks to the presence of nitrogen vacancies.[43,44] Therefore, g-C_3N_4 nanosheets used to prepare the present samples have been synthesized to promote the presence of such defects (see Methods), as determined by Electron Paramagnetic Resonance (EPR) experiments (see Figure S4). The presence of nitrogen vacancies result in the appearance of an EPR signal related to the number of unpaired electron directly correlated to the defect formation.[44] We estimated 4.5×10^{15} paramagnetic centers per gram of sample.

From a quantitative point of view, previously reported NH_3 production rates of pure g-C_3N_4 or of heterojunctions including g-C_3N_4, are higher than those obtained here. However, it is important to stress a delicate point related to the method employed to measure the

photogenerated NH_3. Currently, most of the reports about ammonia production by nitrogen fixation make use of colorimetric methods which are known to be possibly affected by several interfering compounds, in particular in presence of a sacrificial agent (which should be removed according to ref. 46 before the analysis) and when employing catalysts containing nitrogen.[45,46] In the present paper, we devised and optimized an analytical method based on ammonia ion selective electrode (ISEE, for the details see the Methods section) to determine the produced ammonia, thus the efficiency of the nitrogen reduction reaction. The ammonia ISE method was preferred to the colorimetric ones (Nessler's reagent method and indophenol blue method) as it is highly sensitive and selective in controlled experimental conditions (temperature, stirring rate, pH, ionic strength, equilibration time) and not affected by the sacrificial agents and/or by-products.

The results reported above demonstrate the suitability of the novel $Cs_2AgBiCl_6$/g-C_3N_4 system for the photocatalytic hydrogen and ammonia production, also showing a different trend in the production rates as a function of composition. To understand the mechanisms underpinning the two reactions and the charge carrier dynamics, we afforded a detailed spectroscopic and computational modelling work.

The UV-Vis absorption spectra and the Tauc plots for the samples of the novel $Cs_2AgBiCl_6$/g-C_3N_4 composite are shown in Figure S5. The band gap of $Cs_2AgBiCl_6$ is 2.67 eV while that of g-C_3N_4 2.78 eV, in agreement with previous reports.[39,40] According to the relative weight ratio in the composite, the gap lies closer to that of the perovskite or the carbon nitride, without significant variations between the values of the two pure compounds.

The normalized photoluminescence spectra of the $Cs_2AgBiCl_6$/g-C_3N_4 systems are reported in Figure 2. The emission is dominated by the broad and intense features of graphitic carbon nitride, even at very high perovskite loading. Such broad spectra, that completely covers the weak perovskite emission, derive from the superimposition of multiple electronic transitions.[47] In particular, three transitions have been modeled in pristine g-C_3N_4: a high energy

one, centered at around 444 nm, which derives from the relaxation of δ* electrons to the LP state, and two low energy transitions centered at 455 and 505 nm. To access these low energy transitions a non-radiative mechanism to populate the π* state is required, thus the structure of the broadband spectrum depends on the efficiency of this process. In previous works, the interplay between the density of defects and the non-radiative population of π* state have been studied and related to the photocatalytic properties of g-C_3N_4.[47] Composites with lead-free perovskite have also been investigated, with particular focus on population of non-radiative states and its impact on photocatalytic efficiency.[18]

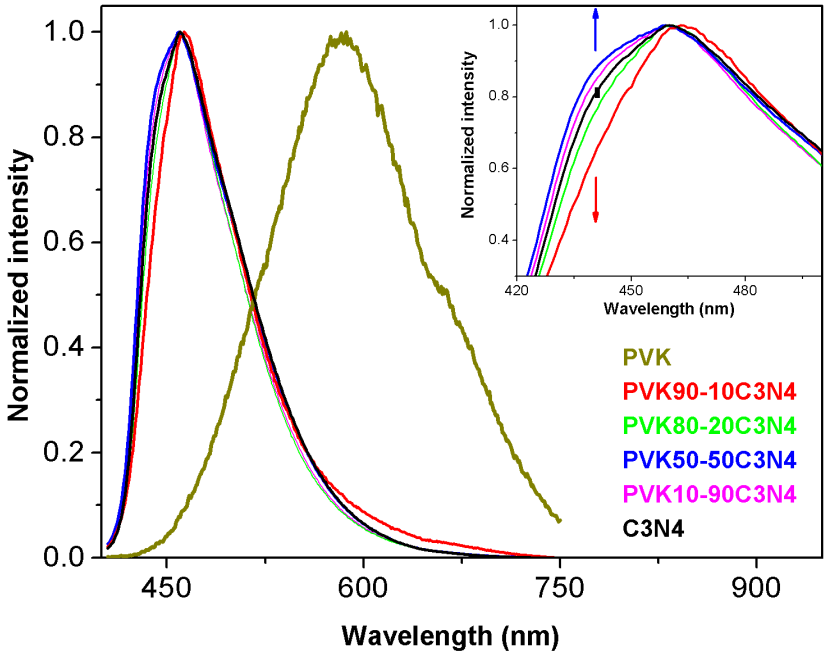

Figure 2. Emission spectra for different $Cs_2AgBiCl_6$/g-C_3N_4 composites
Emission spectra of $Cs_2AgBiCl_6$/g-C_3N_4 composites powders at different percentages of perovskite loading (wt%). g-C_3N_4 and $Cs_2AgBiCl_6$ refer to pristine materials. λ_{ex} = 375 nm. Inset: zoom on an interesting spectral zone. PVK stays for $Cs_2AgBiCl_6$.

On close inspection of the spectral region around the emission band peak (inset of Figure 2), it appears that for low loading of perovskite in the composites there was a reduction of low-lying sub-band population, as the emission displays a stronger contribution from the high energy transition. Conversely, by increasing the perovskite content, the low energy transitions became more and more pronounced. In Figure 2 we reported only representative samples, but

the composite 90-10 $Cs_2AgBiCl_6$-g-C_3N_4 with the best HER performance was also the sample with the weaker contribution to the broad band by the $\delta^* \rightarrow$ LP state transition. These observation points out on the effect of perovskite inclusion in funneling optical excitations to the sites where they can be exploited in photocatalytic processes.

Differential Transmission (DT) measurements were also performed to study how the excited state dynamics depended on $Cs_2AgBiCl_6$/g-C_3N_4 composition. Optical excitations were injected with 100-femtosecond laser pulses, 360 nm in wavelength and 1kHz in repetition rate. A white light supercontinuum was employed as broadband probe (see Supporting Information for experimental details). DT was directly performed on the solutions, with the same concentration used for photocatalytic studies, *i.e.* 1g/L in the case of H_2 production (Fig. 3a) and 0.5 g/L in the case of NH_3 production (Fig. 3b).

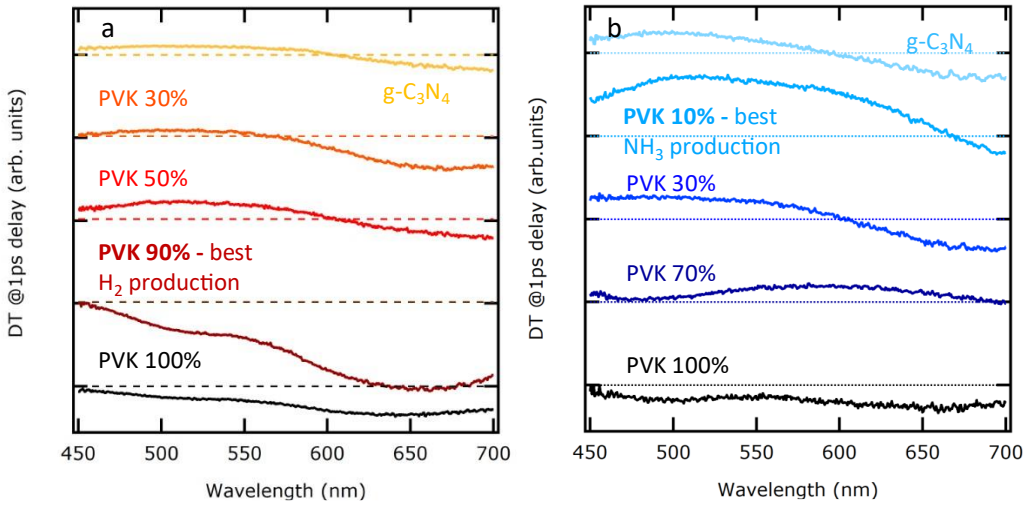

Figure 3 - DT spectra at short time delay (1ps) for different $Cs_2AgBiCl_6$/g-C_3N_4 composites. **a** Results ranging from 100% $Cs_2AgBiCl_6$ perovskite (black line) to 100% g-C_3N_4 (yellow line), with the 90-10 PVK-gC_3N_4 case corresponding to the best HER. **b** Results ranging from 100% $Cs_2AgBiCl_6$ perovskite (black line) to 100% g-C_3N_4 (light-blue line) highlighting the one with 10-90 PVK-gC_3N_4, corresponding to the best nitrogen reduction. Spectra are reported on the same scale, with zero offset for better readability, with dashed horizontal lines representing the zero for the spectrum of the same color. PVK stand for $Cs_2AgBiCl_6$.

Full spectrograms obtained from a DT measurement are reported in Figure S6, while relevant DT spectra extracted at 1 ps delay are reported in Fig. 3. The DT spectrum for the pure

perovskite sample is characterized by a broadband photoinduced absorption feature, due to absorption from excited states. The 90-10 $Cs_2AgBiCl_6$-g-C_3N_4 composite optimized for H_2 generation has an enhanced photoinduced signal with respect to the 100% perovskite sample. This suggests that g-C_3N_4 helps in keeping optical excitations in the perovskite and the HER happens at perovskite sites.

On the other hand, in samples optimized for nitrogen reduction, shown in Figure 3b, the signal is maximum in the case 10-90 $Cs_2AgBiCl_6$-g-C_3N_4, which is the one giving the highest NH_3 production rate. Opposite to what inferred from Figure 3a, in this case the response is the analogous to that of g-C_3N_4, but with an enhanced signal. This suggests that ammonia generation happens at graphitic carbon nitride sites, but the concentration of optical excitations in carbon nitride and thus the ammonia generation rate are enhanced by the presence of perovskite with respect to pure g-C_3N_4.

As a general observation, the combination between g-C_3N_4 and the perovskite enhances the DT signal of the component actively involved in the reaction. Measurements were repeated for different compositions, and the maximum value of the DT signal was extracted for the two different features of the spectrum, i.e., the one at 500-520 nm and the one at 630-650 nm, as reported in Figure 4. In the case of composites optimized for HER, the spectrum mainly consists of photoinduced absorption (negative DT, thus positive differential absorption DA=-DT) and evolves on a picosecond timescale, as shown in Figure 4a.

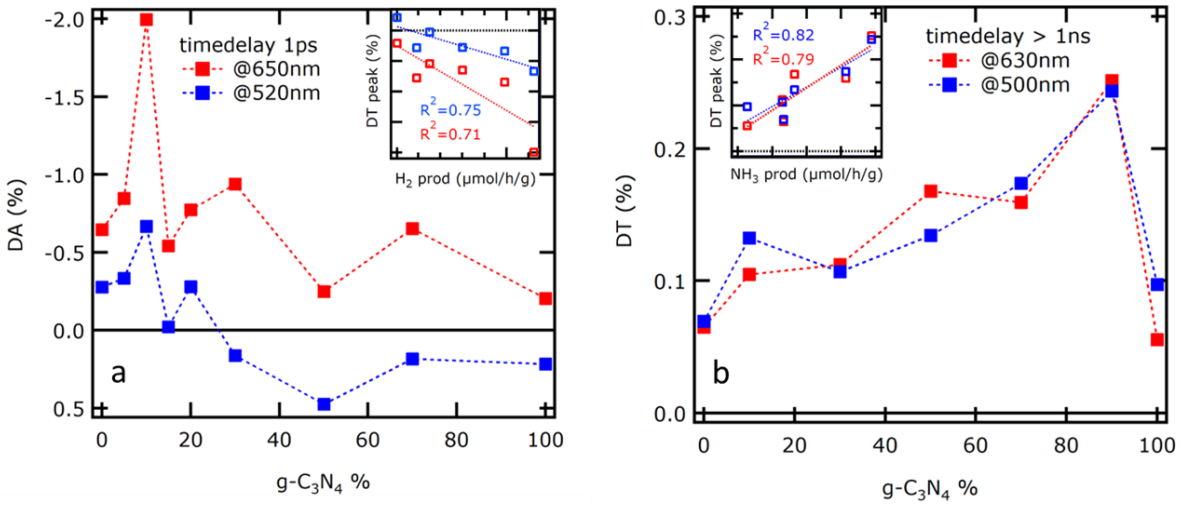

Figure 4 - Correlation between DT amplitude and production rate. a Maximum of DA (DT with a minus sign) extracted at 1ps time delay for different composites as a function of g-C_3N_4 amount. **b** Maximum of DT extracted at time delay >1ns. The colors of markers are indicating the DA (DT) wavelength ranges 500-520 nm region (blue) and 630-650 nm (red). The insets show the linear correlation between DT peaks amplitude and production rates, with R^2 linear correlation coefficients, with the same color legends as the main plots.

Interestingly, the trend of the DA signal as a function of composition was closely related to the trend of HER efficiency. In the case of composites optimized for ammonia generation, a relevant correspondence was found instead between the NH_3 production efficiency and the peak of DT signal at long time delay (above 1ns), as shown in Figure 4b. This observation confirms that for NH_3 production photoinjected carriers, which are always generated in the perovskite, are transferred to the g-C_3N_4, where the ammonia evolution reaction occurs, within a nanoseconds timescale. Additional relevant data reporting the whole DT decay for different compounds and spectra extracted at longer time delay can be found in Supporting Information (Figures S7 and S8).

We performed density functional theory (DFT) calculations to rationalize the trends in hydrogen and ammonia production rates with varying g-C_3N_4 concentration, Figure 1c. All calculations have been carried out at high level of accuracy using hybrid PBE0 functional for geometry optimization with refined HSE06+SOC calculations for single point energies, as

summarized in the Supporting Information. We start with consideration of the pure $Cs_2AgBiCl_6$ phase. Notably, the standalone $Cs_2AgBiCl_6$ generates a substantial amount of hydrogen, Figure 1c. Recent studies have pointed out halide vacancies as potential defects controlling the hydrogen production in the bromide-based analogue $Cs_2AgBiBr_6$.[48,49] Theoretical studies further showed low formation energies of chloride vacancies, V_{Cl}, in $Cs_2AgBiCl_6$ bulk phases.[50] We modeled chloride vacancies in different charge states at a (001)-surface of $Cs_2AgBiCl_6$ with $(Ag_{0.5}Bi_{0.5})Cl_2$-termination, see Figure S9 and Table S2. Our calculations predict deep (+/-) transition levels for a surface V_{Cl} at 1.7 eV above the valence band maximum, see Figure 5a. V_{Cl} in its negative charge state forms a stable Bi-Ag dimer by trapping 2 electrons, see Figure 5d and Figure S10. These electrons are localized at surface defects and likely are key for the hydrogen evolution, as previously reported for Sn-Sn dimers in tin-halide perovskites.[15] The respective (+/-) transition further matches fairly with the experimental photoinduced signals, Figures 3a and 4a. Furthermore, our DFT calculations predict the formation of self-trapped excitons, see Figure S11 and Table S3, being - together with emission from halide vacancies - responsible for the broad emission features in the pure $Cs_2AgBiCl_6$ phase, Figure 2, in line with previous reports.[51–53]

To rationalize the trend in HER, we study the band alignment of the g-C_3N_4/$Cs_2AgBiCl_6$ heterostructure for the $Cs_2AgBiCl_6$ with and without the g-C_3N_4 monolayer adsorbed, representative for the low and high-wt% of g-C_3N_4 regions, respectively; see Figure 5a and Figure S12 for model setup. The band edges of $Cs_2AgBiCl_6$ at the g-C_3N_4 /$Cs_2AgBiCl_6$ interface appears favorable for charge separation, as the conduction band minimum (CBM) of g-C_3N_4 lies energetically lower (3.27 eV) than the one of g-C_3N_4 /$Cs_2AgBiCl_6$ (2.86 eV), in line with the density of states of the heterostructure model, Figure S12c. This results in electron transfer from the perovskite absorber to g-C_3N_4. Moreover, a large offset in band edges of the g-C_3N_4/$Cs_2AgBiCl_6$ to the $Cs_2AgBiCl_6$ itself is present, suggesting a driving force for electrons

from the interface to the $Cs_2AgBiCl_6$ bulk. Increasing the amount of g-C_3N_4 may consequently increase the lifetime of charge carriers due to efficient charge separation, but also suppresses the formation of STEs as seen experimentally, Figure 2, resulting in the increase in HER, Figure 1c.

Our DFT calculations of the g-C_3N_4/$Cs_2AgBiCl_6$ heterostructure shows a strong binding of the g-C_3N_4 on the $(Ag_{0.5}Bi_{0.5})Cl_2$-terminated $Cs_2AgBiCl_6$ surface with a formation energy of -4.22 eV/nm^2, mediated by formation nitrogen-metal bonds with average bond length of 3.09 and 3.23 Å for N-Ag and N-Bi, respectively, see Figure 5b. Consequently, reactive V_{Cl} surface sites are passivated upon increase of g-C_3N_4 and further proton transport to the $Cs_2AgBiCl_6$ surface may be effectively hindered, reducing the evolution of H_2. Note that already a small wt% of g-C_3N_4 may be sufficient to cover the $Cs_2AgBiCl_6$ surface to a large extent, as we estimated from a toy model based on geometrical considerations, see Figure S13. Controlling the wt% of g-C_3N_4 consequently results in an ideal composition that balances efficient charge separation and carrier lifetime as well as the access to active catalytic sites, thereby maximizing the hydrogen evolution rate.

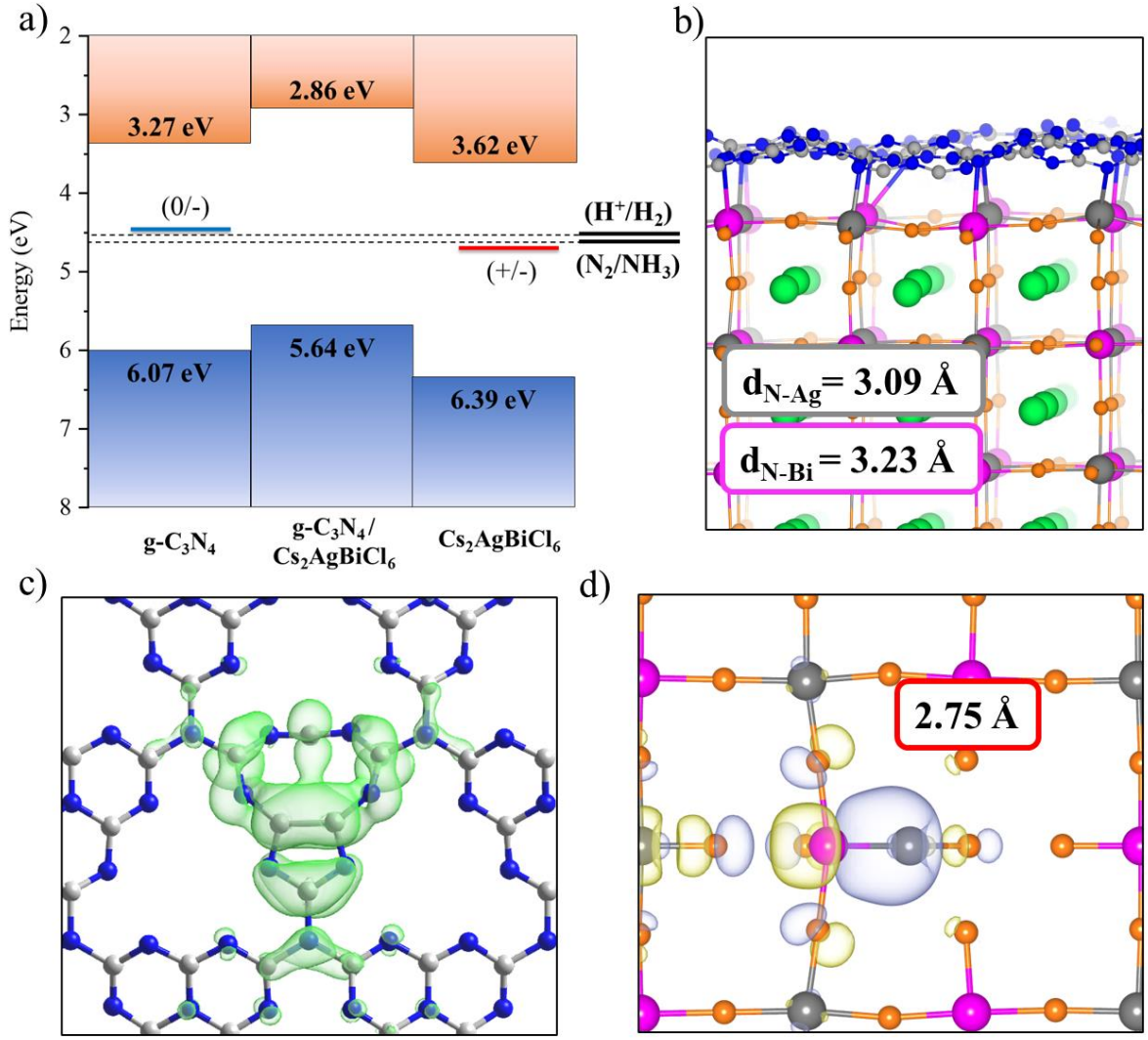

Figure 5. Computational modelling results for the $Cs_2AgBiCl_6$/ g-C_3N_4 heterojunction.
a Band alignment of g-C_3N_4, $Cs_2AgBiCl_6$ and the g-C_3N_4/$Cs_2AgBiCl_6$ interface. H^+/H_2 and N_2/NH_3 redox levels as well as thermodynamic transition levels for the nitrogen vacancy, V_N, and the chloride vacancy, V_{Cl}, are explicitly visualized in the respective phases. Values are referred to the vacuum level. **b** Optimized g-C_3N_4/$Cs_2AgBiCl_6$ interface reporting the average bond lengths for N-Ag and N-Bi. **c** Isodensity plot of the unoccupied state of the neutral nitrogen vacancy V_N responsible for electron trapping in the g-C_3N_4. **d** Isodensity plot of the localized state related to the negatively charged V_{Cl}^-, resulting in the formation of a Ag-Bi dimer with 2.75 Å bond length.

Considering the rate of NH_3 production, we observe a different trend compared to H_2 production, Figure 1c. Initially, the presence of g-C_3N_4 alone is sufficient to generate few amounts of NH_3. Considering the band alignment, electrons should jump from the $Cs_2AgBiCl_6$ to the g-C_3N_4. As potential active sites, we calculate the formation of nitrogen vacancy in g-C_3N_4, resulting in V_N^0 formation energies of 3.36 eV, see Table S4, which is in good agreement

with previous studies.[54–56] The nitrogen vacancy introduces localized energy levels within the band gap, see Figure S14, and introduces a (0/-) transition at 1.56 eV, see Table S5. Importantly, the (0/-) level of nitrogen vacancies are close to the redox potential for N_2/NH_3 (reported by dashed line), suggesting a plausible way for the initial steps in the photofixation mechanism. Upon addition of $Cs_2AgBiCl_6$, the catalytic activity is enhanced which we may attribute to the superior absorbance of the Cs2AgBiCl6 perovskite. At highest perovskite concentration, surface defects of the Cs2AgBiCl6 likely compete with the electron transfer to g-C_3N_4, limiting NH_3 production. This observation highlights the delicate balance required for optimal performance in the heterostructure system, requiring a fine tuning of the heterostructure composition.

Conclusions

$Cs_2AgBiCl_6$/g-C_3N_4 heterojunctions for hydrogen photogeneration and nitrogen reduction to ammonia have been investigated through advanced spectroscopy and computational modelling, aiming at unveiling the mechanism of these reactions. TAS provided detailed information on the charge carried dynamics in the heterojunction indicating that for high perovskite amounts (best performing compositions for H_2 photogeneration) the optical excitations are confined on the $Cs_2AgBiCl_6$, where the reaction occurs. The opposite situation is found for low $Cs_2AgBiCl_6$ (high g-C_3N_4) containing systems (best performing compositions for nitrogen reduction) where the typical DT signal of g-C_3N_4 results to be enchanted. This finding suggests that active sites for ammonia production are confined in the carbon nitride. The trend of DA signal as a function of the composition well follows the trend of the two photocatalytic reactions. DFT calculations show that the active sites for HER are of chloride vacancies, V_{Cl}, and that the coupling to g-C_3N_4, thanks to a favorable band alignment at the interface, increases the lifetime of charge carriers and suppress STE of $Cs_2AgBiCl_6$. The positive effect of the heterojunction formation in promoting hydrogen photogeneration is however progressively lost

by increasing the amount of g-C_3N_4 due to a passivating effect of the V_{Cl}. Such mechanistic insight correlates well with the trend of HER of the $Cs_2AgBiCl_6$ /g-C_3N_4 heterojunction and confirms the active role of the perovskite in this reaction. On the other hand, DFT calculations confirm the role of nitrogen vacancies as the active sites for nitrogen reduction. Herein the positive effect of small perovskite amounts is mostly related to its superior light absorbance, while further increase of $Cs_2AgBiCl_6$amounts progressively reduces the ammonia generation rate promoting the charge funneling towards perovskite active sites, in good agreement with experimental results.

Overall, this study on photoactive heterojunctions including a perovskite and graphitic carbon nitride provides a detailed microscopic insight into the reaction mechanisms, pointing out the key role of the heterostructure composition tuning tailoring different photocatalytic reactions.

Methods

Sample Synthesis, Structural and Morphological Characterization

Nanosheets g-C_3N_4 has been synthesized from the bulk form (bulk g-C_3N_4) with a polymerization of Dicyandiamine DCD ($NH_2C(=NH)NHCN$, Aldrich, 99%) by the following thermal treatment under N_2 flux: heating (1 °C min^{-1}) to a selected temperature of 550 °C, the isothermal step for 4 hours followed by cooling to room temperature (10 °C min^{-1}). The synthesis was carried out in a partially closed alumina crucible. The thermal exfoliated catalyst (nanosheets) was prepared by heating to a selected temperature of 500 °C with an isothermal step for 2h the bulk g-C_3N_4 in air. The $Cs_2AgBiCl_6$/nanosheets g-C_3N_4 composite has been synthesized dissolving a stoichiometric ratio of the precursor salts AgCl (Aldrich 99%), $BiCl_3$ (Aldrich 99%) and CsCl (Aldrich 99%) in organic solvent *N*,*N*-dimethylformamide (DMF) and dried under vigorous stilling at 65 °C. This polar solvent can dissolve most organic and inorganic salts and may be suitable for the cations that are insoluble in HCl. The composites series have been realized changing the percentage of the perovskite ($Cs_2AgBiCl_6$) and the nanosheets g-C_3N_4 (g-C_3N_4 ns) in the composites: 100% $Cs_2AgBiCl_6$, 90% $Cs_2AgBiCl_6$ -10% g-C_3N_4, 80% $Cs_2AgBiCl_6$ -20% g-C_3N_4 ns, 50% $Cs_2AgBiCl_6$ -50% g-C_3N_4 ns, 30% $Cs_2AgBiCl_6$ -70% g-C_3N_4 ns, 10% $Cs_2AgBiCl_6$ -90% g-C_3N_4 ns. The crystal structure of the samples has been characterized by room temperature Cu-radiation XRD acquired with Bruker D2 diffractometer. DRS spectra were acquired in the wavelength range 300-800 nm directly on the powders by using a Jasco V-750 spectrophotometer, equipped with an integrating sphere (Jasco ISV-922). Microstructural characterization of the samples was made using a high-resolution scanning electron microscope (SEM, TESCAN Mira 3) operated at 25 kV.

Hydrogen Evolution Experiments

H_2 evolution experiments were conducted in 37% HCl-50% H_3PO_2 (5:1, v/v) (concentrated acids were from Aldrich)solutions irradiated in Pyrex glass containers (36 mL capacity, 24 mL sample). After addition of the catalyst (1 g L^{-1}), the sample was deoxygenated by Ar bubbling (20 min) to obtain anoxic conditions and irradiated under magnetic stirring for 4 hours. Chloroplatinic acid (H_2PtCl_6, 38% Pt basis) was added as precursor for metallic Pt (Aldrich). Since Pt is *in situ* photodeposited on the catalyst surface, after Ar bubbling a small volume from a 14 g L^{-1} H_2PtCl_6 aqueous solution was added by a 10-100 µL micropipette to the catalyst suspension (1 g L^{-1}), corresponding to 3% w/w Pt. Each photoreactor was closed with sleeve

stopper septa and irradiated, as described in the following, achieving simultaneous Pt deposition and H_2 production.[57]

Irradiation was performed under simulated sola light (1500 W Xenon lamp, 300-800 nm) using a Solar Box 1500e (CO.FO.ME.GRA S.r.l., Milan, Italy) set at a power factor 500 W m^{-2}, and equipped with UV outdoor filter made of IR-treated soda lime glass. Triplicate photoproduction experiments were done on all samples. The headspace evolved gas was quantified by gas chromatography coupled with thermal conductivity detection (GC-TCD), as detailed in previous work.[58] The results obtained in terms of H_2 evolution rate (HER) are expressed in the paper as µmol of gas *per* gram of catalyst *per* hour (µmole g^{-1} h^{-1}). The kinetics of H_2 formation, studied for the best performing composite through duplicate experiments, is reported in Figure S9. The photon flux measured as previously reported, was 1.53×10^{-7} photons moles s^{-1}.[59] The apparent quantum yield (AQY), calculated as the percent ratio H_2 moles/incident photons moles was 2.3% for the composite giving the highest H_2 evolution.[59]

Nitrogen Photofixation Experiments

N_2 photofixation experiments were conducted in tridistilled water containing 10% (v/v) methanol (Aldrich, ≥99.9%) irradiated in Pyrex glass container (250 mL capacity, 100 mL sample). After addition of the catalyst (0.5 g L^{-1}), the sample suspension was deoxygenated by N_2 bubbling (45 min) to obtain a saturated solution and then irradiated under magnetic stirring for 3 hours maintaining the temperature at 15 °C. For the experiments involving use of 1 wt % Pt co-catalyst, the same Chloroplatinic acid (H_2PtCl_6, 38% Pt basis) was added as precursor for metallic Pt (Aldrich).

The quantification was performed with ammonia ion selective electrode, as reported below.

10N NaOH, 10% v/v MeOH) until a stable potential value (mV) was obtained (at least 2 or 3 minutes). For the quantification, a calibration curve was daily constructed plotting the mV value recorded against the Log Concentration, to verify the slope (varying in the range - 54 ÷ -60 mV). The ammonia concentration in the sample was further assessed by two standard additions. Figure S10 reports an example of mean calibration curve (0.25 mg L^{-1} ÷ 10 mg L^{-1} as NH_3). The influence of different parameters was carefully investigated to exclude any possible interferences on the quantification of ammonia in solution.

Sample colour and turbidity did not affect the ISE quantification, as experimentally verified by measurements on both filtered and not-filtered sample obtaining not significantly different NH_3 concentration ($p < 0.05$). Therefore, the final method was applied to not filtered sample. On the

contrast, coloured or cloudy solutions lead to an overestimation of the NH_3 concentration in spectrophotometric assays.

The effect of methanol used as sacrificial agent and its by-products, namely formaldehyde and formic acid, was evaluated by constructing calibration curves. Accordingly, standard solutions were prepared in presence of MeOH in the range 1 ÷ 20 % v/v, HCHO in the range 0.01 mg L^{-1} ÷ 10 and formic acid 0.001 ÷ 0.1 % v/v, respectively. The slope of each curve was compared with the one obtained in ultrapure water, achieving not significantly different values ($p < 0.05$). On the contrast, when using the colorimetric Nessler's reagent method, methanol interferes heavily , resulting in an overestimation of the NH_3 concentration and herein experimentally verified.[46]

Ag and Bi leaching tests

The leaching tests were performed by dispersion of the perovskite powder in distilled water, under magnetic stirring for 4 h. Then the suspension was filtered on 0.2 µm nylon membrane and the amount of Ag and Bi in solution was determined by ICP-OES, after acidification (1% v/v ultrapure nitric acid). The $Cs_2AgBiCl_6$ perovskite resulted stable, with a leaching < 0.1 % for Ag and < 0.05 % for Bi. As silver could interfere by complexing ammonia, leaching tests were also performed on all the g-C_3N_4/$Cs_2AgBiCl_6$ composites, highlighting a negligible Ag release (< 0.9 %) also for the best performing material with negligible complex formation, further confirmed by ISE measurements, in NaOH/EDTA in place of NaOH solution.

Ultrafast spectroscopy measurements

Differential Transmission (DT) measurements were performed on the composite solution in a pump and probe configuration. Ti:Sapphire laser (Libra – Coherent) delivering 100-fs pulses at 800nm with 1kHz repetition rate is sent to a tunable parametric optic amplifier (TOPAS - Light Conversion) to get pulses at the chosen excitation wavelength (360nm). The measurement is performed with two different configurations to explore two different delay range:

- Helios (Ultrafast Systems) with optical delay line (max 8 ns delay), where supercontinuum white probe pulses are derived by focusing the 800nm laser on a Sapphire crystal, thus allowing for sub-ps resolution.
- EOS (ultrafast Systems) with digitally controlled delay (max 1ms delay), with white probe pulses generated by means of a fibre laser.

DT transmitted and reference spectra are collected with two spectrometers coupled to CMOS detectors, in differential configuration. The samples are analysed in form of solution, which is

first sonicated for 15 minutes and then poured into a 1-mm thick quartz cuvette. The concentration of the composites is the same used for the photocatalytic measurements, i.e. 1g/L in the case of HER and 0.5g/L in the case of NH_3 photofixation.

Density functional theory calculations

Computational Details

Density functional theory (DFT) calculations have been carried out for the $Cs_2AgBiCl_6$ and g-C_3N_4 phases, the interface, and defect in the supercell approach. Ionic positions were optimized using the CP2K software package using the PBE0 exchange-correlation functional, and by including DFT-D3 dispersion corrections.[60–63] For g-C_3N_4, we employ an orthorhombic 2×2×2 supercell with a=7.08 Å, b=12.27 Å, c=6.97 Å; for $Cs_2AgBiCl_6$, we use the cubic phase with a=b=c=10.77 Å.[17,39] In all cases, geometry optimization was carried out at the Γ-point of the Brillouin zone. We used the Goedecker-Teter-Hutter (GTH) norm-conserving pseudopotentials and MOLOPT double-zeta Gaussian basis sets.[64,65] The auxiliary density matrix method has been used to accelerate calculations with the hybrid PBE0 functional.[66]

To refine the defect formation energies and thermodynamic ionizations levels, single point DFT calculations were carried out using the hybrid HSE06 functional with inclusion of spin orbit coupling (SOC) corrections on the optimized geometries within the Quantum Espresso software package.[67] Screening of the fraction of exact exchange of the $Cs_2AgBiCl_6$ shows best agreement at a value of α=0.31 with the experimental values, as shown in Table S1. All calculations were carried out at the Γ point of the Brillouin zone, using norm conserving full relativistic pseudopotentials with electrons from Cl 5s, 5p; Cs 5s, 5p, 6s; Ag 5s, 5p, 4d; and Bi 6s, 6p, 5d shells explicitly included. Plane-wave basis set cutoffs for the smooth part of the wave functions and the Fock grid of 40 and 80 Ry, respectively, were chosen. Dispersion corrections were accounted for using the D3 scheme.

Defect formation energies (DFEs) and thermodynamic ionization levels (TILs) were calculated within the supercell approach following the expressions:

$$\mathrm{DFE}[\mathrm{X}^q] = E[\mathrm{X}^q] - E[\mathrm{pristine}] - \sum_i n_i\mu_i + q(\varepsilon_{\mathrm{VB}} + \varepsilon_{\mathrm{F}}) \qquad \text{Eq (1)}$$

$$\varepsilon(q/q') = \frac{\mathrm{DFE}(\mathrm{X}^q|E_{\mathrm{F}}=0) - \mathrm{DFE}(\mathrm{X}^{q'}|E_{\mathrm{F}}=0)}{q'-q} \qquad \text{Eq (2)}$$

where $E[X^q]$ is the energy of the supercell with defect X in the charge state q, E(pristine) is the energy of the pristine (non-defective) supercell. n_i and μ_i are the number and the chemical potentials of the species added or subtracted, respectively and ε_{VB} is the valence band energy of the pristine system.[68] The last two terms of Eq (1) represent the energy to the exchange electrons with the Fermi level of the system (ε_F).

Model setup

Firstly, we optimized the pristine structure of g-C_3N_4 using a 3x2 supercell, see Figure S11a. The monolayer was cut along the (001) direction, and an additional 15 Å of vacuum was added perpendicular to the monolayer to prevent interactions with periodic replicas. Similarly, we optimize a slab model of the double perovskite $Cs_2AgBiCl_6$ using a 2×2 in-plane supercell, with (001) direction, and added 15 Å of vacuum to maintain separation from periodic images. Two different surface terminations were investigated for $Cs_2AgBiCl_6$: $(Ag_{0.5}Bi_{0.5})Cl_2$ and CsCl, see Figure S11b.

Chloride Vacancies in CABC

Considering the $Cs_2AgBiCl_6$, we specifically investigate a chloride vacancy on the $(Ag_{0.5}Bi_{0.5})Cl_2$-terminated surface. The vacancy was stable in the positive charge state (+1), and its presence did not significantly alter the lattice structure of $Cs_2AgBiCl_6$. Upon addition of electrons, we observe the formation of an Ag–Bi dimer. In the neutral state, the dimer shows a distance of 2.82 Å, while in the negatively charged state the distance is reduced to 2.75 Å, shown in Figure S12. The thermodynamic ionization levels (TILs) for the (+/0) and (+/–) transitions are 1.75 eV and 1.69 eV above the valence band maximum, respectively, indicating a deep trap state associated with the defect, see Table S4. As highlighted in the main text of our research, this specific defect holds significant implications as an active site for H_2 production.
We further investigate the geometry of the V_{Cl}^- on the $Cs_2AgBiCl_6$ surface upon inclusion of SOC corrections, as SOC could potentially destabilize the formation of metal dimers as known for the lead-halide perovskites.[69] We optimize the structure containing the V_{Cl}^- vacancy using PBE+SOC within the Quantum Espresso software package. Comparison of the PBE0 and PBE+SOC optimized structures suggest the stability of the Ag-Bi dimer, with bond lengths only slightly varying, see Figure S12. Thus, we can confidently trust the PBE0 structural properties despite neglecting SOC.

Self-trapped excitons

We investigate the formation of self-trapped excitons (STEs) upon illumination. Figure S13a summarizes the STE formation mechanism. Optimizing the system in the triplet state, using the PBE0 functional, results in the localization of the exciton, see Figure S13b. The localization of the electron Kohn-Sham orbital is accompanied by an increase in Bi-Cl bond lengths from 2.7 Å to above 3.0 Å, see Figure S13b. Similarly, the hole Kohn-Sham orbital localized within strongly shortened axial Ag-Cl bonds of 2.3 Å, see Figure S13b. The calculated emission signal is of 1.46 eV while the estimated absorption is at 2.8 eV, see Table S3. Note that halide vacancies likely strongly contribute to the emission. Self-trapping of excitons is key to observe broad emission features, while the detailed contribution of STEs or by recombination from halide vacancies is still under debate.[70,71]

Interface Model

Finally, we model the interface between the g-C_3N_4 and $Cs_2AgBiCl_6$ to gain insight into the structural and electronic modifications upon interface formation. The lattice constants of g-C_3N_4 and $Cs_2AgBiCl_6$ nicely match along the a direction, while the b direction shows substantial differences in the lattice constants of 13%. Thus, we cut the g-C_3N_4 layer along the b-direction and passivate undercoordinated N atoms with H atoms, see Figure S14b. This ensures maximal coverage without introducing artificial strain into the g-C_3N_4. Considering the electronic properties, we obtain a band gap of 3.22 eV for the modified g-C_3N_4, which is in excellent agreement with the fully periodic g-C_3N_4 monolayer (3.4 eV). We passivated both surfaces in the perovskite slab with the modified g-C_3N_4 layers. We initially performed single point calculations at different distances between the $Cs_2AgBiCl_6$ and the g-C_3N_4, as well as for different horizontal alignment for g-C_3N_4. Starting from the low energy configuration, geometry optimization was performed, resulting in a strongly bound heterostructure with a binding energy of -4.22 eV/nm^2. Looking closer at the structure shows that each undercoordinated surface metal ion is successfully passivated (see Figure S14a and Figure 5b of the manuscript). The DOS shown in Figure S14c shows a type II band alignment with the VB and CB of g-C_3N_4 below the ones of the perovskite layer.

The large binding energy presents an interesting hypothesis that may explain the observed drop in the H_2 production rate when adding a small weight percentage of g-C_3N_4. To estimate the surface coverage, we derive a simple toy system relying on pure geometric considerations, shown in Figure S15b. We assume cubic nanocrystals of $Cs_2AgBiCl_6$. The nanocrystal surface area is given by $6L^2$, where L represents the nanocubes dimension. The g-C_3N_4 is modeled as 2D rectangular layers, which may passivate the surfaces of the perovskite nanocubes. The given

wt% of g-C_3N_4 allows us to calculate the surface ratio of the $Cs_2AgBiCl_6$ to the g-C_3N_4, as shown in Figure S13a. Our model system indicates that substantial coverage of the nanocrystal surface can already be achieved at low wt%. This suggests that the passivation of the surface may inhibit the catalytic active site of $Cs_2AgBiCl_6$ due to a small amount of g-C_3N_4.

Nitrogen Vacancies in g-C_3N_4

In g-C_3N_4, three nitrogen atoms can be removed to create vacancies: N1, nitrogen being bonded to three carbon atoms connecting three heptazine flakes; N2, nitrogen being bonded to only two C atoms; and N3, nitrogen being removed from inside a heptazine sub-structure. To determine the most stable state, we considered the neutral state of the vacancy and examined the various possible spin states. Our analysis reveals that the N3 vacancy in a doublet spin state is the most stable, as shown in Table S4.

We further determine the thermodynamic ionization level of N2 and N3 vacancies by calculating the negative charge state by adding an electron. DFEs provide insights into the thermodynamic stability and formation abilities of specific defects. On the other hand, TILs represent the redox potential associated with the capture of carriers at defect sites. For both defects considered, the (0/-) transition is found to be deep within the band gap, see Table S5. This implies that the nitrogen vacancies can trap electrons, localized state within the band gap of the monolayer, as shown in Figure S16. For the monolayer, a band gap value of 3.4 eV was calculated, significantly larger than the experimental values of 2.7 eV due to the reduction in dimensionality. To estimate the accuracy of given defects, we calculate the DFEs and TILs of all nitrogen vacancies in a g-C_3N_4 bulk supercell at same level of theory. The obtained bulk band gap value of 2.9 eV closely aligns with the experimental values, shown in Table S3. Defect TILs remain deep in the band gap, while being shifted downwards in energy.

Declaration of interests

The authors declare no competing interests.

Acknowledgement

L.M., A.S., A.P. acknowledge support from the Ministero dell'Università e della Ricerca (MUR) and the University of Pavia through the program "Dipartimenti di Eccellenza 2023–2027. L.M., E.M. and A.L. acknowledge support from the Ministero dell'Università e della Ricerca (MUR) through PRIN Project REVOLUTION (2022HRZH7P). A. P. acknowledges

support from the Ministero dell'Università e della Ricerca (MUR) through PRIN Project PHOTOFIX (2022TWKM4X). E.M. and S.C. acknowledge project Ricerca@Cnr PHOTOCAT (CUP B93C21000060006). F.D.A. acknowledges funds by the European Union - NextGenerationEU under the Italian Ministry of University and Research (MUR) National Innovation Ecosystem grant ECS00000041 - VITALITY. S.C. acknowledges support from the Ministero dell'Università e della Ricerca (MUR) through PRIN Project INTERFACE (2022HWWW3S). L.M. and C.T. acknowledge financial support from R.S.E. SpA (Ricerca sul Sistema Energetico).

References

1. Huang, H., Pradhan, B., Hofkens, J., Roeffaers, M. B. J. & Steele, J. A. Solar-Driven Metal Halide Perovskite Photocatalysis: Design, Stability, and Performance. *ACS Energy Lett.* **5**, 1107–1123 (2020).
2. Huynh, K. A. *et al.* Halide perovskite photocatalysis: progress and perspectives. *Journal of Chemical Technology & Biotechnology* **95**, 2579–2596 (2020).
3. Bresolin, B.-M., Park, Y. & Bahnemann, D. W. Recent Progresses on Metal Halide Perovskite-Based Material as Potential Photocatalyst. *Catalysts* **10**, 709 (2020).
4. Corti, M. *et al.* Application of Metal Halide Perovskites as Photocatalysts in Organic Reactions. *Inorganics* **9**, 56 (2021).
5. Yuan, J., Liu, H., Wang, S. & Li, X. How to apply metal halide perovskites to photocatalysis: challenges and development. *Nanoscale* (2021) doi:10.1039/D0NR07716J.
6. Temerov, F., Baghdadi, Y., Rattner, E. & Eslava, S. A Review on Halide Perovskite-Based Photocatalysts: Key Factors and Challenges. *ACS Appl. Energy Mater.* **5**, 14605–14637 (2022).
7. Xiao, M. *et al.* Addressing the stability challenge of metal halide perovskite based photocatalysts for solar fuel production. *J. Phys. Energy* **4**, 042005 (2022).
8. Chen, Z.-Y., Huang, N.-Y. & Xu, Q. Metal halide perovskite materials in photocatalysis: Design strategies and applications. *Coordination Chemistry Reviews* **481**, 215031 (2023).
9. Romani, L. & Malavasi, L. Solar-Driven Hydrogen Generation by Metal Halide Perovskites: Materials, Approaches, and Mechanistic View. *ACS Omega* **5**, 25511–25519 (2020).
10. Armenise, V., Colella, S., Fracassi, F. & Listorti, A. Lead-Free Metal Halide Perovskites for Hydrogen Evolution from Aqueous Solutions. *Nanomaterials* **11**, 433 (2021).

11. Wang, J., Shi, Y., Wang, Y. & Li, Z. Rational Design of Metal Halide Perovskite Nanocrystals for Photocatalytic CO_2 Reduction: Recent Advances, Challenges, and Prospects. *ACS Energy Lett.* **7**, 2043–2059 (2022).
12. Raza, M. A., Li, F., Que, M., Zhu, L. & Chen, X. Photocatalytic reduction of CO_2 by halide perovskites: recent advances and future perspectives. *Mater. Adv.* **2**, 7187–7209 (2021).
13. Wang, X., He, J., Chen, X., Ma, B. & Zhu, M. Metal halide perovskites for photocatalytic CO2 reduction: An overview and prospects. *Coordination Chemistry Reviews* **482**, 215076 (2023).
14. Tedesco, C. & Malavasi, L. Bismuth-Based Halide Perovskites for Photocatalytic H2 Evolution Application. *Molecules* **28**, 339 (2023).
15. Ricciarelli, D. *et al.* Reaction Mechanism of Photocatalytic Hydrogen Production at Water/Tin Halide Perovskite Interfaces. *ACS Energy Lett.* 1308–1315 (2022) doi:10.1021/acsenergylett.2c00122.
16. Romani, L. *et al.* PEA2SnBr4: a water-stable lead-free two-dimensional perovskite and demonstration of its use as a co-catalyst in hydrogen photogeneration and organic-dye degradation. *J. Mater. Chem. C* **8**, 9189–9194 (2020).
17. Romani, L. *et al.* Water-Stable DMASnBr3 Lead-Free Perovskite for Effective Solar-Driven Photocatalysis. *Angewandte Chemie International Edition* **60**, 3611–3618 (2021).
18. Romani, L. *et al.* Experimental Strategy and Mechanistic View to Boost the Photocatalytic Activity of $Cs_3Bi_2Br_9$ Lead-Free Perovskite Derivative by g-C_3N_4 Composite Engineering. *Adv. Funct. Mater.* **31**, 2104428 (2021).
19. Bresolin, B.-M., Günnemann, C., Bahnemann, D. W. & Sillanpää, M. Pb-Free Cs3Bi2I9 Perovskite as a Visible-Light-Active Photocatalyst for Organic Pollutant Degradation. *Nanomaterials* **10**, 763 (2020).

20. Park, S. *et al.* Photocatalytic hydrogen generation from hydriodic acid using methylammonium lead iodide in dynamic equilibrium with aqueous solution. *Nat Energy* **2**, 16185 (2017).
21. Pisanu, A. *et al.* Enhanced air-stability of Sn-based hybrid perovskites induced by dimethylammonium (DMA): synthesis, characterization, aging and hydrogen photogeneration of the MA1−xDMAxSnBr3 system. *J. Mater. Chem. C* **7**, 7020–7026 (2019).
22. Li, K. *et al.* Highly-efficient and stable photocatalytic activity of lead-free Cs2AgInCl6 double perovskite for organic pollutant degradation. *Journal of Colloid and Interface Science* **596**, 376–383 (2021).
23. Zhou, L., Xu, Y.-F., Chen, B.-X., Kuang, D.-B. & Su, C.-Y. Synthesis and Photocatalytic Application of Stable Lead-Free $Cs_2AgBiBr_6$ Perovskite Nanocrystals. *Small* **14**, 1703762 (2018).
24. Jiang, Y., Zhou, R., Zhang, Z., Dong, Z. & Xu, J. Boosted charge transfer and CO_2 photoreduction by construction of S-scheme heterojunctions between $Cs_2AgBiBr_6$ nanosheets and two-dimensional metal–organic frameworks. *J. Mater. Chem. C* **11**, 2540–2551 (2023).
25. Cheng, S. *et al.* In-situ growth of Cs2AgBiBr6 perovskite nanocrystals on Ti3C2Tx MXene nanosheets for enhanced photocatalytic activity. *Applied Surface Science* **621**, 156877 (2023).
26. Huang, H. *et al.* Metal Halide Perovskite Based Heterojunction Photocatalysts. *Angew Chem Int Ed* **61**, (2022).
27. Mishra, R. *et al.* A review on Z/S – scheme heterojunction for photocatalytic applications based on metal halide perovskite materials. *Applied Surface Science Advances* **9**, 100241 (2022).

28. Yang, J., Wang, D., Han, H. & Li, C. Roles of Cocatalysts in Photocatalysis and Photoelectrocatalysis. *Acc. Chem. Res.* **46**, 1900–1909 (2013).
29. Paul, T. *et al.* CsPbBrCl2/g-C3N4 type II heterojunction as efficient visible range photocatalyst. *Journal of Hazardous Materials* **380**, 120855 (2019).
30. Xie, B. *et al.* Fabrication of an FAPbBr3/g-C3N4 heterojunction to enhance NO removal efficiency under visible-light irradiation. *Chemical Engineering Journal* **430**, 132968 (2022).
31. Bai, Z.-J. *et al.* Tuning photocatalytic performance of Cs3Bi2Br9 perovskite by g-C3N4 for C(sp3)—H bond activation. *Nano Res.* (2022) doi:10.1007/s12274-022-4835-z.
32. Corti, M. *et al.* g-C $_3$ N $_4$ /metal halide perovskite composites as photocatalysts for singlet oxygen generation processes for the preparation of various oxidized synthons. *Catal. Sci. Technol.* **11**, 2292–2298 (2021).
33. Wang, Y. *et al.* Lead-free perovskite Cs2AgBiBr6@g-C3N4 Z-scheme system for improving CH4 production in photocatalytic CO2 reduction. *Applied Catalysis B: Environmental* **282**, 119570 (2021).
34. Zhang, M., Wang, W., Gao, F. & Luo, D. g-C3N4-Stabilised Organic–Inorganic Halide Perovskites for Efficient Photocatalytic Selective Oxidation of Benzyl Alcohol. *Catalysts* **11**, 505 (2021).
35. Medina-Llamas, M. *et al.* Preparation of Heterojunctions Based on Cs3Bi2Br9 Nanocrystals and g-C3N4 Nanosheets for Photocatalytic Hydrogen Evolution. *Nanomaterials* **13**, 263 (2023).
36. Ismael, M. & Wu, Y. A mini-review on the synthesis and structural modification of g-C $_3$ N $_4$ -based materials, and their applications in solar energy conversion and environmental remediation. *Sustainable Energy Fuels* **3**, 2907–2925 (2019).

37. Guan, Z. *et al.* Perovskite photocatalyst CsPbBr3-xIx with a bandgap funnel structure for H2 evolution under visible light. *Applied Catalysis B: Environmental* **245**, 522–527 (2019).

38. Huang, Q., Guo, Y., Chen, J., Lou, Y. & Zhao, Y. NiCoP modified lead-free double perovskite $Cs_2AgBiBr_6$ for efficient photocatalytic hydrogen generation. *New J. Chem.* **46**, 7395–7402 (2022).

39. McClure, E. T., Ball, M. R., Windl, W. & Woodward, P. M. Cs_2AgBiX_6 (X = Br, Cl): New Visible Light Absorbing, Lead-Free Halide Perovskite Semiconductors. *Chem. Mater.* **28**, 1348–1354 (2016).

40. Wang, X. *et al.* A metal-free polymeric photocatalyst for hydrogen production from water under visible light. *Nature Mater* **8**, 76–80 (2009).

41. Wang, T., Yue, D., Li, X. & Zhao, Y. Lead-free double perovskite Cs2AgBiBr6/RGO composite for efficient visible light photocatalytic H2 evolution. *Applied Catalysis B: Environmental* **268**, 118399 (2020).

42. Jiang, Y. *et al.* In Situ Synthesis of Lead-Free Halide Perovskite $Cs_2AgBiBr_6$ Supported on Nitrogen-Doped Carbon for Efficient Hydrogen Evolution in Aqueous HBr Solution. *ACS Appl. Mater. Interfaces* **13**, 10037–10046 (2021).

43. Cheng, M., Xiao, C. & Xie, Y. Photocatalytic nitrogen fixation: the role of defects in photocatalysts. *J. Mater. Chem. A* **7**, 19616–19633 (2019).

44. Dong, G., Ho, W. & Wang, C. Selective photocatalytic N_2 fixation dependent on g-C_3N_4 induced by nitrogen vacancies. *J. Mater. Chem. A* **3**, 23435–23441 (2015).

45. Huang, R. *et al.* Recent advances in photocatalytic nitrogen fixation: from active sites to ammonia quantification methods. *RSC Adv.* **11**, 14844–14861 (2021).

46. Zhao, Y. *et al.* Ammonia Detection Methods in Photocatalytic and Electrocatalytic Experiments: How to Improve the Reliability of NH_3 Production Rates? *Adv. Sci.* **6**, 1802109 (2019).

47. Sharma, A., Varshney, M., Chae, K. H. & Won, S. O. Mechanistic investigations on emission characteristics from g-C3N4, g-C3N4@Pt and g-C3N4@Ag nanostructures using X-ray absorption spectroscopy. *Current Applied Physics* **18**, 1458–1464 (2018).
48. Zhang, S. *et al.* Surface defect-induced electronic structures of lead-free Cs2AgBiBr6 double-perovskite for efficiently solar-driven photocatalytic performance. *Applied Surface Science* **609**, 155446 (2023).
49. He, Z. *et al.* Lead-Free $Cs_2AgBiBr_6$ Perovskite with Enriched Surface Defects for Efficient Photocatalytic Hydrogen Evolution. *Energy Fuels* **35**, 15005–15009 (2021).
50. Xu, J., Liu, J., Liu, B., Wang, J. & Huang, B. Defect Engineering of Grain Boundaries in Lead-Free Halide Double Perovskites for Better Optoelectronic Performance. *Adv Funct Materials* **29**, 1805870 (2019).
51. Palummo, M., Berrios, E., Varsano, D. & Giorgi, G. Optical Properties of Lead-Free Double Perovskites by Ab Initio Excited-State Methods. *ACS Energy Lett.* **5**, 457–463 (2020).
52. Luo, J. *et al.* Efficient and stable emission of warm-white light from lead-free halide double perovskites. *Nature* **563**, 541–545 (2018).
53. Zhang, L. *et al.* Tuning Emission and Electron–Phonon Coupling in Lead-Free Halide Double Perovskite $Cs_2AgBiCl_6$ under Pressure. *ACS Energy Lett.* **4**, 2975–2982 (2019).
54. Raciti, E. *et al.* Radical defects modulate the photocatalytic response in 2D-graphitic carbon nitride. *Chem. Sci.* **13**, 9927–9939 (2022).
55. Liu, X. *et al.* Structural, electronic and photocatalytic properties of g-C3N4 with intrinsic defects: A first-principles hybrid functional investigation. *Applied Surface Science* **499**, 143994 (2020).
56. Huang, P. *et al.* Carbon and vacancy centers in hexagonal boron nitride. *Phys. Rev. B* **106**, 014107 (2022).

57. Huang, J., Nie, G. & Ding, Y. Metal-Free Enhanced Photocatalytic Activation of Dioxygen by g-C3N4 Doped with Abundant Oxygen-Containing Functional Groups for Selective N-Deethylation of Rhodamine B. *Catalysts* **10**, 6 (2019).
58. Speltini, A. *et al.* Sunlight-promoted photocatalytic hydrogen gas evolution from water-suspended cellulose: a systematic study. *Photochem Photobiol Sci* **13**, 1410–1419 (2014).
59. Speltini, A., Romani, L., Dondi, D., Malavasi, L. & Profumo, A. Carbon Nitride-Perovskite Composites: Evaluation and Optimization of Photocatalytic Hydrogen Evolution in Saccharides Aqueous Solution. *Catalysts* **10**, 1259 (2020).
60. VandeVondele, J. *et al.* Quickstep: Fast and accurate density functional calculations using a mixed Gaussian and plane waves approach. *Computer Physics Communications* **167**, 103–128 (2005).
61. Adamo, C. & Barone, V. Toward reliable density functional methods without adjustable parameters: The PBE0 model. *The Journal of Chemical Physics* **110**, 6158–6170 (1999).
62. Perdew, J. P., Ernzerhof, M. & Burke, K. Rationale for mixing exact exchange with density functional approximations. *The Journal of Chemical Physics* **105**, 9982–9985 (1996).
63. Grimme, S., Antony, J., Ehrlich, S. & Krieg, H. A consistent and accurate *ab initio* parametrization of density functional dispersion correction (DFT-D) for the 94 elements H-Pu. *The Journal of Chemical Physics* **132**, 154104 (2010).
64. Goedecker, S., Teter, M. & Hutter, J. Separable dual-space Gaussian pseudopotentials. *Phys. Rev. B* **54**, 1703–1710 (1996).
65. VandeVondele, J. & Hutter, J. Gaussian basis sets for accurate calculations on molecular systems in gas and condensed phases. *The Journal of Chemical Physics* **127**, 114105 (2007).
66. Guidon, M., Hutter, J. & VandeVondele, J. Auxiliary Density Matrix Methods for Hartree−Fock Exchange Calculations. *J. Chem. Theory Comput.* **6**, 2348–2364 (2010).

67. Giannozzi, P. *et al.* QUANTUM ESPRESSO: a modular and open-source software project for quantum simulations of materials. *Journal of Physics: Condensed Matter* **21**, 395502 (2009).
68. Van De Walle, C. G. & Neugebauer, J. First-principles calculations for defects and impurities: Applications to III-nitrides. *Journal of Applied Physics* **95**, 3851–3879 (2004).
69. Meggiolaro, D. & De Angelis, F. First-Principles Modeling of Defects in Lead Halide Perovskites: Best Practices and Open Issues. *ACS Energy Lett.* **3**, 2206–2222 (2018).
70. Kahmann, S. *et al.* The Origin of Broad Emission in ⟨100⟩ Two-Dimensional Perovskites: Extrinsic vs Intrinsic Processes. *ACS Energy Lett.* **7**, 4232–4241 (2022).
71. Morana, M. *et al.* Origin of Broad Emission Induced by Rigid Aromatic Ditopic Cations in Low-Dimensional Metal Halide Perovskites. *J. Phys. Chem. Lett.* 7860–7868 (2023) doi:10.1021/acs.jpclett.3c01872.